Supporting materials for:

Photoelectron Spectroscopy of Wet and Gaseous Samples through Electron Transparent Graphene Membranes

*Jürgen Kraus[1], Robert Reichelt[1], Sebastian Günther[1], Luca Gregoratti[2], Matteo Amati[2], Maya Kiskinova[2], Alexander Yulaev[3,5], Ivan Vlassiouk [4] and Andrei Kolmakov[5]**

[1]Technische Universität München D-85748 Garching, Germany

[2] Sincrotrone Trieste 34012 Trieste, Italy

[3]Department of Materials Science and Engineering, University of Maryland, College Park, MD 20742, USA

[4] Oak Ridge National Laboratory, Oak Ridge, TN 37831, USA

[5] Center for Nanoscale Science and Technology, NIST, Gaithersburg, MD 20899, USA

*To whom correspondence should be sent: andrei.kolmakov@nist.gov

1) Graphene grown on Cu - preparation protocols and crystalline quality:

Three different protocols were used to grow g-Cu samples (g-Cu-1, g-Cu-2 and g-Cu-3) to optimize the quality of CVD graphene. All samples were grown as monolayer graphene, but their crystalline quality varied as evidenced by Raman spectroscopy. The lowest crystalline quality sample, g-Cu-1, was used for attenuation tests in the μ-probe x-ray photoelectron spectroscopy (μ-PES) experiment. It contained monolayer graphene with a substantial amount of bilayer islands and defects as indicated from Raman spectroscopy (see below). The second sample g-Cu-

2 was monolayer graphene from which single layer suspended g-membranes were fabricated and characterized by scanning electron microscopy (SEM) and μ-PES. The third g-Cu-3 sample was grown after the μ-PES measurements in order to perform photoelectron attenuation tests in using a standard XPS system.

The three g-Cu samples were prepared by chemical vapor deposition (CVD) in a reactive CH_4/H_2 gas atmosphere. Prior to the growth, Cu foil pretreatment at elevated temperature in pure hydrogen was carried out. The applied pretreatment conditions affect the nucleation density of the graphene patches[48, 67]. The mixing ratio $w = H_2 / CH_4$ determine the growth velocity by balancing the etching and growth rate and thus the crystalline quality of the formed graphene layer.[68] Each temperature increase (5 K/min) was performed in pure hydrogen at the flow conditions in the following annealing step. For g-Cu-1 and g-Cu-2 the pressure in the reactor was regulated by controlling the hydrogen flow, for g-Cu-3 in addition the conductance of the tubes and thus the pump speed of the reactor system were changed in order to vary the pressure at a given gas flow. The applied protocols are listed in Table S1.

As noted in the text of the manuscript, Raman spectroscopy was used to characterize the crystalline quality of the grown graphene layers.[69, 70] The corresponding spectra are compiled in Figure S1. The presence of a D-band indicates, whether defects, domain boundaries or flake

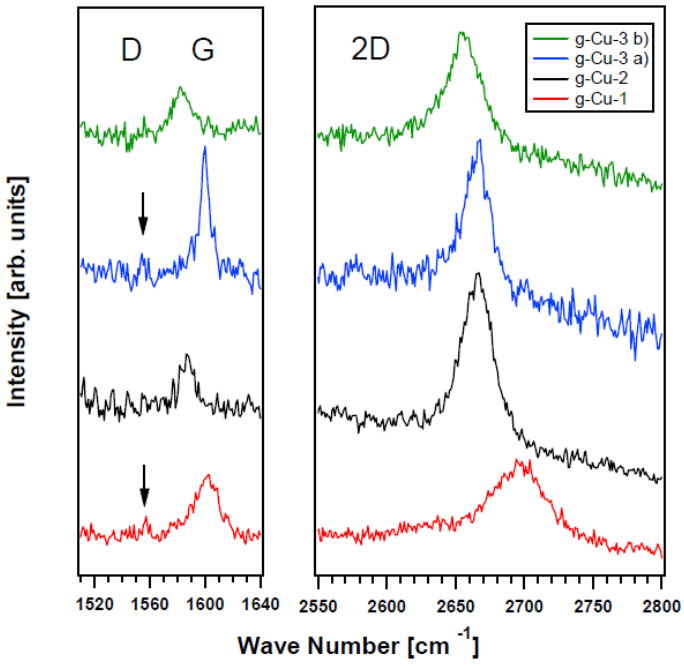

Figure S1: Raman spectra indicating the different crystalline quality of the samples g-Cu-1 (monolayer graphene with substantial amount of disorder as indicated by the presence of a D-band and the large FWHM of the G and 2D band). g-Cu-2 monolayer graphene as clearly evidenced by the acquired G and 2D band. Even improved quality was observed for graphene flakes grown in hydrogen rich atmospheres (g-Cu-3a). Gradual increase of the methane concentration during growth led to full graphene coverage formation, but the crystalline graphene quality suffered slightly (g-Cu-3b).

edges exist in the grown film. The intensity ratio $I_{2D}/I_G > 2$ was found to be valid for all of the samples indicating that mainly monolayer graphene was grown. The large FWHM = 52 cm^{-1} of the 2D band obtained from g-Cu-1 indicates that either bilayer graphene flakes or differently stressed graphene is present in the film which contained graphene grain boundaries (small D-band, see arrow). On the other hand, g-Cu-2 consists of high quality monolayer graphene indicative by the sharp 2D band (FWHM = 26 cm^{-1}). High quality graphene with single crystalline flakes is achieved when growing in a hydrogen rich reactive atmosphere.[71] Stopping the CVD process after growth at w = H_2/CH_4 = 100 as done for sample g-Cu-3a),

graphene flakes were formed from which a Raman spectrum with a narrow G- and a sharp 2D band (FWHM = 23 cm^{-1}) could be acquired. (The formation of graphene flakes was observed in SEM. For the correct positioning of the laser spot during the Raman measurements the graphene flakes were made visible for optical microscopy by slightly oxidizing the Cu surface surrounding the graphene islands according to the recipe reported in [67]). The presence of a small D-band indicates that the spot covered part of the flake boundary (see arrow in the corresponding spectrum of Figure S1). The formation of a fully graphene covered Cu foil was achieved by gradually increasing the methane concentration during growth as verified by SEM. The modified preparation protocol g-Cu-3 b) is listed in Table S1. Raman spectroscopy showed that full coverage formation took place at the cost of crystalline graphene quality as shown by the slightly larger 2D band width (FWHM = 32 cm^{-1}) of the spectrum displayed in Figure S1. The attenuation tests using the standard laboratory x-ray source were performed using the fully coverage graphene film g-Cu-3.

g-Cu-1						
preparation	**time (min)**	**T (°C)**	**p (mbar)**	**H_2-flow (sccm)**	**CH_4-flow (sccm)**	**w = H_2 /CH_4**
pretreatment	60	800	1	1.5	--	--
growth	20	1000	1.4	1.5	0.5	**3**

g-Cu-2						
preparation	**time (min)**	**T (°C)**	**p (mbar)**	**H_2-flow (sccm)**	**CH_4-flow (sccm)**	**w = H_2 /CH_4**
pretreatment	60	1000	0.3	1.5	--	--

growth	30	1000	0.3	1.5	0.15	**10**
	30	1000	0.4	1.5	0.30	**5**

g-Cu-3 a) g-flake						
preparation	**time (min)**	**T (°C)**	**p (mbar)**	**H_2-flow (sccm)**	**CH_4-flow (sccm)**	**w = H_2 /CH_4**
pretreatment	5	840	0.3	5	--	--
	10	840	50	10	--	--
	40	950	50	10	--	--
	1	950	0.3	1	--	--
growth	60	950	0.3	1	0.01	**100**

g-Cu-3 b) g-fully covered						
preparation	**time (min)**	**T (°C)**	**p (mbar)**	**H_2-flow (sccm)**	**CH_4-flow (sccm)**	**w = H_2 /CH_4**
pretreatment	5	840	0.3	5	--	--
	10	840	50	10	--	--
	40	950	50	10	--	--
	1	950	0.8	15	--	--
growth	30	1000	0.8	15	0.15	**100**
	30	1000	0.8	15	0.30	**50**
	30	1000	0.8	15	0.45	**33**
	30	1000	0.8	15	0.60	**25**

	30	1000	0.9	15	3.00	**5**

Table S1: Preparation protocols for the sample g-Cu-1, g-Cu-2 and g-Cu-3. The growth of the sample g-Cu-3 involved a stepwise pretreatment in order to flatten the surface and the graphene growth in a hydrogen rich atmosphere with a hydrogen-methane ratio of w = 100. When stopping the growth single graphene flakes with high crystalline quality were grown (a). For full coverage graphene formation the methane content of the reactive atmosphere was increased stepwise during growth (b).

2) Preparation protocol of suspended graphene via controlled back side Cu etching

For the preparation of pristine suspended g-membranes which have the least possible amount of contaminants a special etching procedure was developed to etch the Cu foil underneath the grown graphene layer without using any lithographic procedures and - more important - without the use of a PMMA protection layer on top of the grown graphene.[71] The Cu foils were pre-structured by applying a lithographic mask and etching small etch pits into the Cu foil at a limited current density of about 100 mA/cm^2. The etching was stopped before micro-holes were formed. Subsequently, the lithography layer was removed and graphene was CVD grown in a custom built quartz glass reactor. Then, the etch pits of the graphene covered Cu foil had to be etched through by globally etching of the Cu foil. This last step was performed without any lithographic layer. For this purpose, the Cu foil was placed on the liquid electrolyte with the grown graphene layer facing towards the surrounding gas atmosphere. A special mechanical mechanism provided electrical contact without applying any force on the Cu foil. The slow electrochemical removal of the Cu surface underneath the graphene layer was controlled by

optical microscopy with an illuminating light source behind the backside of the sample. The Cu etching was interrupted after the first holes appeared in the Cu foil, which was easily done by observing transmitted light from the backside illumination. The electrolyte was carefully exchanged, first with water and afterwards with acetone and the Cu foil was removed from the liquid. Without a protection layer most of the graphene membranes collapse upon drying due to capillary forces, however some membranes survived. Since no any PMMA coverage was used, these membranes have the advantage of being very clean with a minimum amount of contaminations from the etching process and provide the highest electron transparency of the studied samples.

Two Cu foils were grown in parallel in the same CVD process g-Cu-2 from which suspended graphene membranes were produced. One sample was immediately characterized by SEM and Raman. On the second foil membrane I, II and III were etched, characterized by SEM and then used for the μ-PES and scanning photoelectron microscopy (SPEM) measurements as discussed in the text of the main paper (these membranes are shown in Figure 4 and Figure S3 and S4). Figure S2 displays two SEM images of the first Cu foil with empty and graphene covered holes, where the membranes collapsed or survived the wet chemical etching procedure, respectively.

The circle in the right SEM image indicates the area of a

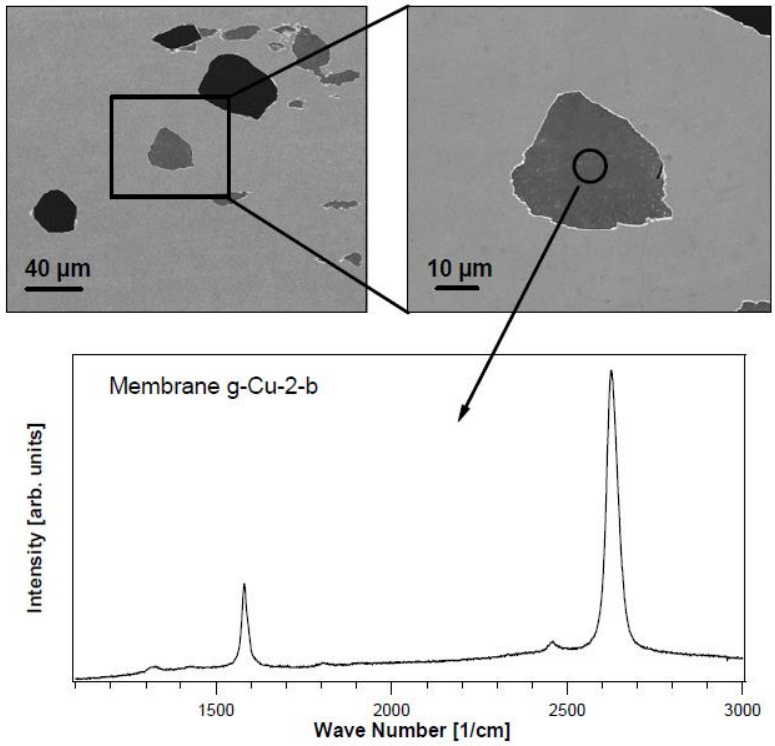

Figure S2: SEM and Raman data acquired from a second g-Cu-2 sample which was grown together with the g-Cu-2 sample used for the µ-PES measurements displayed in Fig. 4 of the main text. The Raman spectrum clearly indicates that the suspended membrane contained monolayer graphene.

membrane from which the displayed Raman spectrum was acquired. In agreement with further data obtained from similarly prepared samples these data clearly indicate that the etched g-Cu membranes contain monolayer graphene. Note that the Raman signal from the suspended graphene membranes is at least one order of magnitude more intense when compared to the supported g-Cu samples (see Figure S1), so that details in the spectrum such as the G* band at 2458 cm^{-1} are visible.[70] The I_{2D}/I_G = 6.35 and the FWHM of the 2D-band = 36 cm^{-1} clearly indicate suspended monolayer graphene. Thus, we can conclude that as well membrane I and II used for the µ-PES measurements of Figure 4 are of monolayer type graphene. The parallel investigation of two Cu foils was necessary, because the repetitive characterization with SEM, the sample preparation before, during and after the µ-PES measurement of the sample g-Cu-2

and the prolonged time in air before and after the measurements at ELETTRA led to a substantial contamination of the corresponding membranes by sp^3 carbon.

3) Evidence of breakage of membrane III and hole- formation in membrane II:

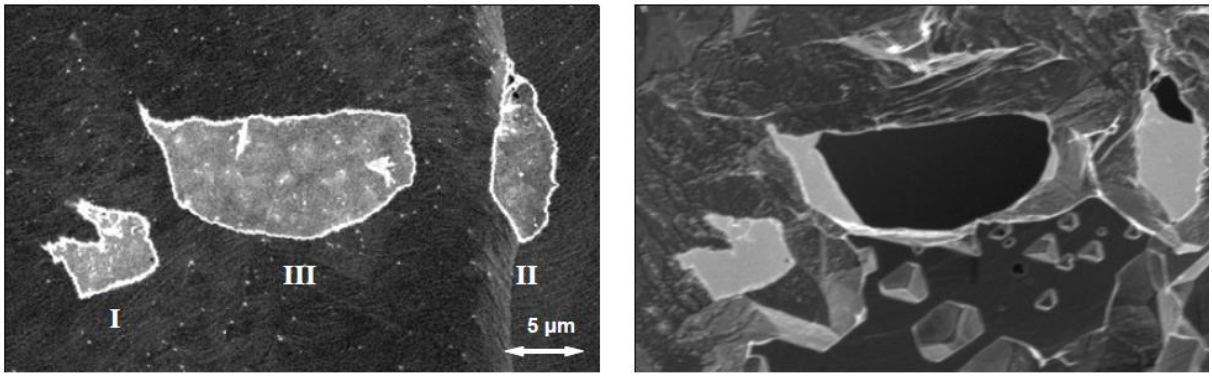

Figure S3: SEM images (primary energy 5 kV) of membrane I, II and III obtained from the sample topside before (left) and the sample backside after the performed SPEM measurements (right). For sake of better visibility the latter image is plotted by mirror scaling the horizontal axis. The data show that during sample handling Membrane III collapsed and membrane II developed a small hole at its top.

Figure S 3 shows an SEM image of membrane I, II and III before (a) and after the performed SPEM measurements at ELETTRA (b). The SEM image acquired after the µ-PES measurements was acquired from the backside of the Cu foil showing the topography of the etch pits close to the through etched hole. For sake of better visibility this image is plotted in a horizontally reversed way. The SEM image clearly evidences that membrane III collapsed during sample handling of the SPEM measurements. That this collapse occurred already during the first mounting of the sample was observed in the SPEM as a lack of any C 1s count rate obtainable from membrane III, i.e. the central membrane appeared black in a C 1s image (see for example Figure 4 of the main text and Figure S4 below). In addition, the right SEM image shows that membrane II developed a small hole at its top. Therefore, the photoemission data discussed in

the main text of the paper were restricted to membrane I and the intact, lower part of membrane II.

4) Relating topographic contrast in the photoemission images to the local surface geometry and estimating the achievable photoelectron yield:

As noted in the text of the manuscript and thoroughly discussed in ref. [72], the contrast in SPEM images is highly related to the inclination of the imaged surface with respect to the irradiating photon beam and the position of the electron analyzer. Here, we outline in detail, how to assign the measured photoelectron intensity to the local geometry of the sample surface. From the data displayed in Figure 4 of the manuscript and acquired after the backside of the membranes had been covered by gold, we can extract the peak intensities obtained from membrane I, II and from the graphene covered Cu surface in the left vicinity of the suspended membranes (position IV). The values are listed in Table S2 and relate to the three locations I, II and IV indicated in Figure S4, which displays area of the g-Cu-2 sample in the vicinity of membrane I and II as imaged by SEM and in the SPEM by acquiring C 1s photo- as well as CuL_3VV auger electrons.

	membrane I		g-Cu position IV		membrane II	
	intensity (counts/sec)	relative intensity	intensity (counts/sec)	relative intensity	intensity (counts/sec)	relative intensity
$I_{C\ 1s}$	5724		5323		12157	

$I_{C\ 1s}$ / $I_{C\ 1s\text{-}membrane\text{-}I}$		1		0.93		2.12
$I_{Au\ 4f}$	8753		30 (= noise level)		32333	
$I_{Au\ 4f}$ / $I_{Au\ 4f\text{-}membrane\text{-}I}$		1		0		3.7
$I_{Cu\ 3p}$	1495		5900		2456	
$I_{Cu\ 3p}$ / $I_{Au\ 4f\text{-}membrane\ I}$		0.17		0.67		0.08

Table S2: The measured intensity of the C 1s, Au 4f and the Cu 3p core level acquired from different locations I, II and IV of the g-Cu-2 sample surface (see Figure 4 and S4).

All three images display a large hole at the top and the area of the three membranes I, II and III below. As shown in the last paragraph with the help of Figure S3, membrane III collapsed before imaging in the SPEM, so it appears dark in the C 1s image with equal (zero) count rate as the large hole. Table S 2 confirms that the C 1s intensity acquired from membrane I nearly equals to the one obtained from the g-Cu surface (position IV). This is expected when considering that monolayer graphene was grown on Cu and that as well the membranes should be made from suspended monolayer graphene (see Figure S2). As a consequence, membrane I should not appear in the C 1s image as long as the geometry of the membrane does not differ from the one

of the surrounding support and background intensity does not influence the image contrast too much. This is indeed the case as visible from the C 1s image in Figure S4. In addition the SEM image shows that position IV and membrane I are both located on the same Cu grain which was aligned perpendicularly to the irradiating photon beam (geometry depicted in the left sketch below the electron image). Since both areas are plan parallel there is no topographic contribution to a SPEM image[72] and the Cu L_3VV image shows a similar dark patch at the position of membrane I and membrane III, since on both location no Cu material is present below the membrane or inside the hole where membrane III has collapsed.

On the other hand, the C 1s signal obtained from the intact part of membrane II is about twice as high as the one from membrane I (see Table S2). After Au evaporation to the sample backside, the intensity of the Au 4f core level was also found to be higher, when being acquired from membrane II. Since the signal increase of both the C1s and the Au 4f core level cannot be caused by an eventual enlarged membrane thickness of the suspended graphene membrane II, we conclude that membrane II is also made of suspended monolayer graphene, but that its surface is inclined with respect to the photon beam.

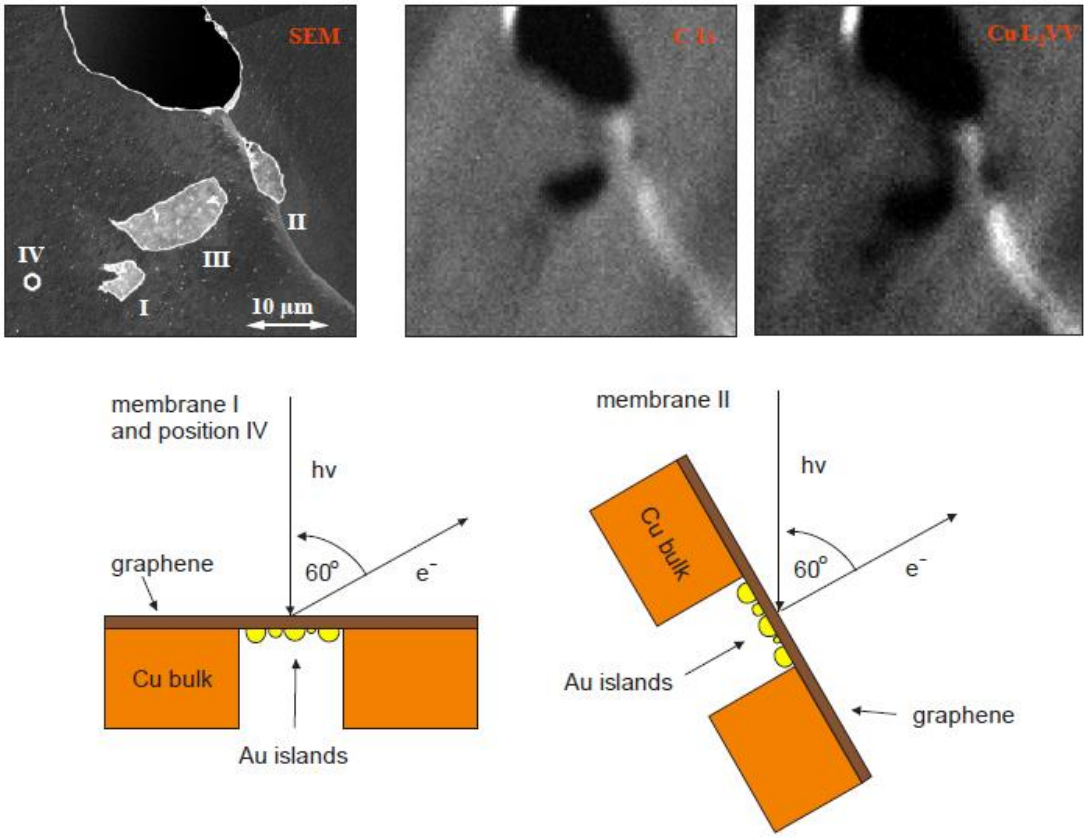

Figure S4: Upper row: SEM and C 1s and Cu L_3VV SPEM images of the g-Cu-2 area around membrane I and membrane II. Lower row: Local geometry of surface plane belonging to membrane I and to membrane II, respectively, with respect to the irradiating photon beam and the electron analyzer.

The SEM image of Figure S4 shows that this inclination results from the fact that membrane II is located at a Cu grain boundary which is highly inclined with respect to the two separated Cu grains. The amount of surface atoms irradiated by the focused photon beam scales with $1/\cos(\theta)$, where θ is the angle between the surface normal and the irradiating photon beam and as a consequence in the inclined case the signal will be enlarged. Since an increase by about a factor of 2 is measured, we conclude that the inclination amounts $\theta = 60°$. The lower right panel of Figure S4 sketches the local geometry of membrane II. As noted in the text of the manuscript, the described intensity increase applies for all sample areas which are inclined in the same way and the grain boundary area appears as a bright rim in both the C 1s and the Cu L_3VV transition

image (see Figure 4 and Figure S4). In the following we show that all other acquired photoelectron intensities of Table S2 are consistent with this geometry. For the performed estimations the following values are used (at the chosen photon energy of 978 eV).[73, 74]

	E_{kin} [eV]	λ_g (graphite) [Å]	λ_{Cu} in Cu [Å]	λ_{Au} in Au [Å]	σ [Mbarn]	β asymmetry
Au 4f	894	27		12.9	0.8	0.959
Cu 3p	903	27	16.3		0.08	1.582

Table S3: Inelastic mean free path, cross sections and asymmetry parameter for the Au 4f and the Cu 3p core level.

For the estimation of the photoelectron intensities the layer distance of d_g = 3.35 Å in graphite is used as estimate of the graphene height above the Cu or Au support. The layer distances in the Cu foil (which is known to be (100) textured)[75-77] is d_{Cu} = 1.8 Å (= (100)-step height). The step height of a (111) step in Au of d_{Au} = 2.36 Å (= (111)-step height) is used as estimate of the layer distance in the Au particles, which were grown on the backside of the membrane. We assume that the gold growth on the suspended graphene membrane follows Volmer-Weber growth as observed for Au on HOPG: It is known that at large coverage the Au grows in a form of large islands on HOPG, which are best characterized by (111) oriented islands, which resemble the shape of truncated octahedrons (or half spheres).[78] At low coverage, the formation of very small Au clusters on HOPG was reported,[52] which deviate from the assumed geometry. Since these small clusters are identified by a shifted Au 4f speak and since such a peak

shift is not observed in our acquired spectra, we can conclude that small Au clusters do not represent a large fraction of the grown Au islands on the backside of the suspended g-membrane. As a consequence, we can safely assume that on the membrane rather large Au islands were formed during the evaporation a room temperature with island height larger than 25 Å. (Island diameters of room temperature grown Au on HOPG of ~100 Å are reported).[78] Table S3 indicates that a gold island height of 25 Å is about twice as large as the inelastic mean free path of the emitted Au 4f photoelectrons. Since the photoelectron signal originating from a depth of 2 λ amounts 86% of the total photoelectron signal from an entire solid, we can estimate the signal contribution from each Au island as the one obtained from bulk gold. With these assumptions we can compare the Au 4f -I and Au 4f-II intensity obtained from membranes I and II, respectively:

$$\frac{I(Au4f-II)}{I(Au4f-I)} = \frac{1}{\cos(60^\circ)} \times \frac{\exp\left(-\frac{d_C}{\lambda_C}\right)}{\exp\left(-\frac{d_C}{\lambda_C \cos(60^\circ)}\right)} \times \frac{1-\exp\left(-\frac{d_{Au}}{\lambda_{Au}\cos(60^\circ)}\right)}{1-\exp(-\frac{d_{Au}}{\lambda_{Au}})}$$

$$= \quad 2 \quad \times \quad 1.13 \quad \times \quad 1.83 \quad = \quad 4.14$$

Here, the first term amounts for the signal increase due to the different inclination of the sample surface with respect to the irradiating photon beam. The second term accounts to the damping of the carbon layer and finally the third term represents the signal contribution from deeper Au layers of the gold islands on the backside of the membrane. Using the values from Table S3 leads to the indicated numbers, which fit well the experimentally observed Au 4f signal increase of a factor of 3.7 (see Table S2). From the above equation, it is clear that the signal increase does not stem from the transparency difference of both membrane, which amounts only a factor 1.13 (i.e. membrane II is about 13 % more transparent due to the changed geometry). The observed signal increase due to the inclined membrane surface is rather caused by the increased amount of surface atoms (a factor of 2.00) and the photoemission from deeper Au layers, which contribute

more strongly to the core level signal in the inclined geometry of membrane II (another factor of 1.83). Note that the limited membrane transparency starts to play a role only when the membrane thickness exceeds about 3-4 layers. Still, due to the increased signal intensity the geometry of membrane II is favorable as discussed in the following.

We can finally calculate which fraction *x* of the membrane was covered by Au islands in the experiment and estimate the detection limit of the membrane devices in the two different geometries of membrane I and II. This can be done when at first relating the observed Cu 3p-g-Cu signal intensity obtained from the flat Cu support to the Au 4f-I intensity acquired from membrane I. Since the kinetic energy of the Cu 3p equals almost the one of the Au 4f photoelectrons the transmission of the electron analyzer can be regarded as constant. Due to the plane parallel surfaces of the g-Cu foil and membrane I the equation greatly simplifies and the fraction x can be extracted:

$$\frac{I(Cu3p-g-Cu)}{I(Au4f-I)} = \frac{100\%}{x\%} \times \frac{\rho(Cu)}{\rho(Au)} \times \frac{\sigma(Cu3p)}{\sigma(Au4f)} \times \frac{1+\beta_{Cu3p} \times 0.625}{1+\beta_{Au4f} \times 0.625} \times \frac{1-\exp\left(-\frac{d_{Au}}{\lambda_{Au}\cos(60^\circ)}\right)}{1-\exp\left(-\frac{d_{Cu}}{\lambda_{Cu}\cos(60^\circ)}\right)}$$

$$= \frac{100\%}{x\%} \times 1.11 \times 0.1 \times 1.24 \times 1.55 = 0.67$$

The first factor beside the relative coverage fraction x addresses the different packing density ρ of the Cu foil and the Au island which can be estimated as the one of a Cu (100) and a Au (111) surface. With the lattice constant of 3.61 Å and 4.08 Å for Cu and Au this leads to a factor of 1.11. All other factors can be calculated using the values listed in Table S3. The difference in photo ionization cross section from the Cu 3p and the Au 4f core level amounts a factor 0.1, the asymmetry factor for the geometry of the experiment leads to a further factor of 1.24 and finally the signal contribution from photoemission from deeper layers for the Cu and for the Au solid

lead to a last factor of 1.55 when considering the inelastic mean free path in the different metal solids. Inserting the relative signal Cu 3p-g-Cu/ Au4f-I intensity of 0.67 (see Table S2) leads to the estimation that about x = 32 % of the membrane backside surface is covered by Au islands. These numbers provide the possibility to estimate the obtainable sensitivity of a photoelectron measurement through such a membrane. Assuming that the Au 4f peak would be significantly detectable when exceeding 3 times the noise level (i.e. count rate ≈100 sec^{-1}) and that the calculated gold loading of 32% on membrane I relates to the obtained Au 4f count rate of 8753 counts/sec, a gold coverage of 32% x100/8753 ≈ 0.4% on the back side of membrane I would still be detectable. With shrinking coverage the islands should shrink and as a consequence as well their thickness would diminish. If islands of a nominal thickness of one atomic layer are reached, the sensitivity would decrease by a factor of $1/(1-\exp(-d_{Au}/\lambda_{Au}\cos(60°)))$ = 3.3 due to the lack of signal contribution from deeper layers. Still about 1% of a monolayer should be detectable. In the more preferable geometry of membrane II the sensitivity would increase by a factor of four. As a result, photoemission experiments through suspended monolayer graphene membranes may reach very high sensitivity of 0.25% to 1 % of a monolayer. We note that many interesting core levels have a cross section of more than a factor of 10 lower than the one of the Au 4f core level. As a consequence, for such core levels the reachable resolution is lower, but still low quantity detection in the submonolayer regime seems feasible. We finally want to point out that the effect of the membrane thickness on the experiment can be estimated with the help of Figure 1 of the manuscript, which easily provides the expected precision which can be reached using a graphene based membrane of given thickness.

References:

1. Knop-Gericke, A.; Kleimenov, E.; Hävecker, M.; Blume, R.; Teschner, D.; Zafeiratos, S.; Schlögl, R.; Bukhtiyarov, V. I.; Kaichev, V. V.; Prosvirin, I. P., *Advances in Catalysis* **2009,** *52*, 213-272.

2. Somorjai, G. A.; York, R. L.; Butcher, D.; Park, J. Y., *Physical Chemistry Chemical Physics* **2007,** *9* (27), 3500-3513. DOI Doi 10.1039/B618805b.

3. Zhang, C.; Grass, M. E.; McDaniel, A. H.; DeCaluwe, S. C.; El Gabaly, F.; Liu, Z.; McCarty, K. F.; Farrow, R. L.; Linne, M. A.; Hussain, Z., *Nature materials* **2010,** *9* (11), 944-949.

4. Lu, Y.-C.; Crumlin, E. J.; Veith, G. M.; Harding, J. R.; Mutoro, E.; Baggetto, L.; Dudney, N. J.; Liu, Z.; Shao-Horn, Y., *Scientific reports* **2012,** *2*.

5. Ghosal, S.; Hemminger, J. C.; Bluhm, H.; Mun, B. S.; Hebenstreit, E. L.; Ketteler, G.; Ogletree, D. F.; Requejo, F. G.; Salmeron, M., *Science* **2005,** *307* (5709), 563-566.

6. Ketteler, G.; Ashby, P.; Mun, B. S.; Ratera, I.; Bluhm, H.; Kasemo, B.; Salmeron, M., *J Phys-Condens Mat* **2008,** *20* (18). DOI Artn 184024

Doi 10.1088/0953-8984/20/18/184024.

7. Siegbahn, H.; Siegbahn, K., *Journal of Electron Spectroscopy and Related Phenomena* **1973,** *2* (3), 319-325.

8. Siegbarn, H.; Asplund, L.; Kelfve, P.; Hamrin, K.; Karlsson, L.; Siegbahn, K., *Journal of Electron Spectroscopy and Related Phenomena* **1974,** *5* (1), 1059-1079.

9. Winter, B.; Faubel, M., *Chemical reviews* **2006,** *106* (4), 1176-1211.

10. Brown, M. A.; Jordan, I.; Redondo, A. B.; Kleibert, A.; Wörner, H. J.; van Bokhoven, J. A., *Surface Science* **2013**.

11. Starr, D. E.; Wong, E. K.; Worsnop, D. R.; Wilson, K. R.; Bluhm, H., *Physical Chemistry Chemical Physics* **2008,** *10* (21), 3093-3098.

12. Siegbahn, H., *The Journal of Physical Chemistry* **1985,** *89* (6), 897-909.

13. Amati, M.; Abyaneh, M. K.; Gregoratti, L., *Journal of Instrumentation* **2013,** *8* (05), T05001.

14. Joyner, R. W.; Roberts, M. W.; Yates, K., *Surface Science* **1979,** *87* (2), 501-509.

15. Ruppender, H.; Grunze, M.; Kong, C.; Wilmers, M., *Surface and interface analysis* **1990,** *15* (4), 245-253.

16. Ogletree, D. F.; Bluhm, H.; Lebedev, G.; Fadley, C. S.; Hussain, Z.; Salmeron, M., *Review of Scientific Instruments* **2002,** *73* (11), 3872-3877.

17. Salmeron, M.; Schlogl, R., *Surf Sci Rep* **2008,** *63* (4), 169-199. DOI DOI 10.1016/j.surfrep.2008.01.001.

18. Starr, D.; Liu, Z.; Hävecker, M.; Knop-Gericke, A.; Bluhm, H., *Chemical Society Reviews* **2013**.

19. Mun, B. S.; Kondoh, H.; Liu, Z.; Ross Jr, P. N.; Hussain, Z., The Development of Ambient Pressure X-Ray Photoelectron Spectroscopy and Its Application to Surface Science. In *Current Trends of Surface Science and Catalysis*, Springer: 2014; pp 197-229.

20. Tao, F., *Chemcatchem* **2012,** *4* (5), 583-590. DOI DOI 10.1002/cctc.201200002.

21. Jurgensen, A.; Esser, N.; Hergenroder, R., *Surface and Interface Analysis* **2012,** *44* (8), 1100-1103. DOI Doi 10.1002/Sia.4826.

22. Roy, K.; Vinod, C.; Gopinath, C. S., *The Journal of Physical Chemistry C* **2013,** *117* (9), 4717-4726.

23. Schnadt, J.; Knudsen, J.; Andersen, J. N.; Siegbahn, H.; Pietzsch, A.; Hennies, F.; Johansson, N.; Martensson, N.; Ohrwall, G.; Bahr, S., *Journal of synchrotron radiation* **2012,** *19* (5), 701-704.

24. Frank Ogletree, D.; Bluhm, H.; Hebenstreit, E. D.; Salmeron, M., *Nuclear Instruments and Methods in Physics Research Section A: Accelerators, Spectrometers, Detectors and Associated Equipment* **2009,** *601* (1), 151-160.

25. Jablonski, A.; Powell, C. J., *Journal of Vacuum Science & Technology A* **2009,** *27* (2), 253-261.

26. Briggs, D.; Seah, M. P., *Practical Surface Analysis by Auger and X-ray Photoelectron Spectroscopy*. John Wiley & Sons Ltd **1983**.

27. Ballarotto, V.; Breban, M.; Siegrist, K.; Phaneuf, R.; Williams, E., *Journal of Vacuum Science & Technology B* **2002,** *20* (6), 2514-2518.

28. Wakita, T.; Taniuchi, T.; Ono, K.; Suzuki, M.; Kawamura, N.; Takagaki, M.; Miyagawa, H.; Guo, F.; Nakamura, T.; Muro, T., *Japanese journal of applied physics* **2006,** *45* (3R), 1886.

29. Kobayashi, K., *Nuclear Instruments and Methods in Physics Research Section A: Accelerators, Spectrometers, Detectors and Associated Equipment* **2009,** *601* (1), 32-47.

30. Masuda, T.; Yoshikawa, H.; Noguchi, H.; Kawasaki, T.; Kobata, M.; Kobayashi, K.; Uosaki, K., *Applied Physics Letters* **2013,** *103* (11), 111605-111605-4.

31. Bryson III, C. E.; Grunthaner, F. J.; Grunthaner, P. J. Electron transmissive window usable with high pressure electron spectrometry. **2004**.

32. Abrams, I. M.; McBain, J. W., *Journal of Applied Physics* **1944,** *15* (8), 607-609. DOI doi:http://dx.doi.org/10.1063/1.1707475.

33. de Jonge, N.; Ross, F. M., *Nat Nano* **2011,** *6* (11), 695-704.

34. Novoselov, K.; Jiang, D.; Schedin, F.; Booth, T.; Khotkevich, V.; Morozov, S.; Geim, A., *Proceedings of the National Academy of Sciences of the United States of America* **2005,** *102* (30), 10451-10453.

35. Park, S.; Ruoff, R. S., *Nature nanotechnology* **2009,** *4* (4), 217-224.

36. Mutus, J.; Livadaru, L.; Robinson, J.; Urban, R.; Salomons, M.; Cloutier, M.; Wolkow, R., *New Journal of Physics* **2011,** *13* (6), 063011.

37. Kolmakov, A.; Dikin, D. A.; Cote, L. J.; Huang, J.; Abyaneh, M. K.; Amati, M.; Gregoratti, L.; Günther, S.; Kiskinova, M., *Nature Nanotechnology* **2011,** *6* (10), 651-657.

38. Stoll, J. D.; Kolmakov, A., *Nanotechnology* **2012,** *23* (50), 505704.

39. Bunch, J. S.; Verbridge, S. S.; Alden, J. S.; van der Zande, A. M.; Parpia, J. M.; Craighead, H. G.; McEuen, P. L., *Nano letters* **2008,** *8* (8), 2458-2462.

40. Yuk, J. M.; Park, J.; Ercius, P.; Kim, K.; Hellebusch, D. J.; Crommie, M. F.; Lee, J. Y.; Zettl, A.; Alivisatos, A. P., *Science* **2012,** *336* (6077), 61-64.

41. Suk, J. W.; Kitt, A.; Magnuson, C. W.; Hao, Y.; Ahmed, S.; An, J.; Swan, A. K.; Goldberg, B. B.; Ruoff, R. S., *ACS nano* **2011,** *5* (9), 6916-6924.

42. Powell, C.; Jablonski, A., *Surface and interface analysis* **2002,** *33* (3), 211-229.

43. Li, X.; Cai, W.; An, J.; Kim, S.; Nah, J.; Yang, D.; Piner, R.; Velamakanni, A.; Jung, I.; Tutuc, E.; Banerjee, S. K.; Colombo, L.; Ruoff, R. S., *Science* **2009,** *324* (5932), 1312-1314.

44. Barinov, A.; Dudin, P.; Gregoratti, L.; Locatelli, A.; Mentes, T. O.; Nino, M. A.; Kiskinova, M., *Nucl Instrum Meth A* **2009,** *601* (1-2), 195-202. DOI DOI 10.1016/j.nima.2008.12.157.

45. Rasool, H. I.; Song, E. B.; Mecklenburg, M.; Regan, B.; Wang, K. L.; Weiller, B. H.; Gimzewski, J. K., *Journal of the American Chemical Society* **2011,** *133* (32), 12536-12543.

46. Cho, J.; Gao, L.; Tian, J.; Cao, H.; Wu, W.; Yu, Q.; Yitamben, E. N.; Fisher, B.; Guest, J. R.; Chen, Y. P., *ACS nano* **2011,** *5* (5), 3607-3613.

47. Gao, L.; Guest, J. R.; Guisinger, N. P., *Nano letters* **2010,** *10* (9), 3512-3516.

48. Kraus, J.; Böcklein, S.; Reichelt, R.; Günther, S.; Santos, B.; Menteş, T. O.; Locatelli, A., *Carbon* **2013,** *64*, 377-390.

49. Tanuma, S.; Powell, C.; Penn, D., *Surface and Interface Analysis* **2011,** *43* (3), 689-713.

50. Xu, M.; Fujita, D.; Gao, J.; Hanagata, N., *Acs Nano* **2010,** *4* (5), 2937-2945.

51. Hövel, H.; Barke, I., *Progress in surface science* **2006,** *81* (2), 53-111.

52. Büttner, M.; Oelhafen, P., *Surface Science* **2006,** *600* (5), 1170-1177. DOI http://dx.doi.org/10.1016/j.susc.2006.01.020.

53. Ketteler, G.; Yamamoto, S.; Bluhm, H.; Andersson, K.; Starr, D. E.; Ogletree, D. F.; Ogasawara, H.; Nilsson, A.; Salmeron, M., *The Journal of Physical Chemistry C* **2007,** *111* (23), 8278-8282.

54. Lange, K. M.; Kothe, A.; Aziz, E. F., *Physical Chemistry Chemical Physics* **2012,** *14* (16), 5331-5338.

55. Stolyarova, E.; Stolyarov, D.; Bolotin, K.; Ryu, S.; Liu, L.; Rim, K.; Klima, M.; Hybertsen, M.; Pogorelsky, I.; Pavlishin, I., *Nano letters* **2008,** *9* (1), 332-337.

56. Xu, K.; Cao, P.; Heath, J. R., *Science* **2010,** *329* (5996), 1188-1191.

57. Grogan, J. M.; Schneider, N. M.; Ross, F. M.; Bau, H. H., *Nano Letters* **2013**. DOI 10.1021/nl404169a.

58. Royall, C.; Thiel, B.; Donald, A., *Journal of Microscopy* **2001,** *204* (3), 185-195.

59. Thiberge, S.; Zik, O.; Moses, E., *Review of Scientific Instruments* **2004,** *75* (7), 2280-2289.

60. Leapman, R. D.; Sun, S., *Ultramicroscopy* **1995,** *59* (1), 71-79.

61. Wang, L.; Travis, J. J.; Cavanagh, A. S.; Liu, X.; Koenig, S. P.; Huang, P. Y.; George, S. M.; Bunch, J. S., *Nano letters* **2012,** *12* (7), 3706-3710.

62. Neto, A.; Novoselov, K., *Materials Express* **2011,** *1* (1), 10-17.

63. Zaera, F., *Chemical Reviews* **2012,** *112* (5), 2920-2986.

64. Li, X.; Zhu, Y.; Cai, W.; Borysiak, M.; Han, B.; Chen, D.; Piner, R. D.; Colombo, L.; Ruoff, R. S., *Nano letters* **2009,** *9* (12), 4359-4363.

65. Abyaneh, M. K.; Gregoratti, L.; Amati, M.; Dalmiglio, M.; Kiskinova, M., *e-Journal of Surface Science and Nanotechnology* **2011,** *9* (0), 158-162.

66. More, J., *Numerical analysis* **1978**, 105-116.

67. Wang, H.; Wang, G.; Bao, P.; Yang, S.; Zhu, W.; Xie, X.; Zhang, W.-J., *Journal of the American Chemical Society* **2012**. DOI 10.1021/ja2105976.

68. Vlassiouk, I.; Regmi, M.; Fulvio, P.; Dai, S.; Datskos, P.; Eres, G.; Smirnov, S., *ACS Nano* **2011,** *5* (7), 6069-6076. DOI 10.1021/nn201978y.

69. Dresselhaus, M. S.; Jorio, A.; Souza Filho, A. G.; Saito, R., *Philosophical Transactions of the Royal Society A: Mathematical, Physical and Engineering Sciences* **2010,** *368* (1932), 5355-5377. DOI 10.1098/rsta.2010.0213.

70. Malard, L. M.; Pimenta, M. A.; Dresselhaus, G.; Dresselhaus, M. S., *Phys. Rep.-Rev. Sec. Phys. Lett.* **2009,** *473* (5-6), 51-87. DOI 10.1016/j.physrep.2009.02.003.

71. Kraus, J.; Böcklein, S.; Reichelt, R.; Günther, S.; Santos, B.; Mentes, T. O.; Locatelli, A., *Carbon* **2013,** *64*, 377-390.

72. Günther, S.; Kolmakov, A.; Kovac, J.; Kiskinova, M., *Ultramicroscopy* **1998,** *75* (1), 35-51.

73. Tanuma, S.; Powell, C. J.; Penn, D. R., *Surface and Interface Analysis* **1991,** *17*, 26.

74. Yeh, J. J.; Lindau, I., *Atomic Data and Nuclear Data Tables* **1985,** *32*, 1-155.

75. Wofford, J. M.; Nie, S.; McCarty, K. F.; Bartelt, N. C.; Dubon, O. D., *Nano Letters* **2010,** *10* (12), 4890-4896. DOI 10.1021/nl102788f.

76. Cho, J.; Gao, L.; Tian, J.; Cao, H.; Wu, W.; Yu, Q.; Yitamben, E. N.; Fisher, B.; Guest, J. R.; Chen, Y. P.; Guisinger, N. P., *ACS Nano* **2011,** *5* (5), 3607-3613. DOI 10.1021/nn103338g.

77. Rasool, H. I.; Song, E. B.; Allen, M. J.; Wassei, J. K.; Kaner, R. B.; Wang, K. L.; Weiller, B. H.; Gimzewski, J. K., *Nano Letters* **2010,** *11* (1), 251-256. DOI 10.1021/nl1036403.

78. Hövel, H.; Barke, I., *Progress in Surface Science* **2006,** *81* (2–3), 53-111. DOI http://dx.doi.org/10.1016/j.progsurf.2006.01.002.